

Minimal Detection Time for Localization of Radioactive Hot Spots in Low and Elevated Background Environments Using a CZT Gamma-Ray Spectrometer

Peer-reviewed author version

BRABANTS, Lowie; SIMONS, Mattias; DE SCHEPPER, David; DEMEESTER, Eric & SCHROEYERS, Wouter (2022) Minimal Detection Time for Localization of Radioactive Hot Spots in Low and Elevated Background Environments Using a CZT Gamma-Ray Spectrometer. In: NUCLEAR TECHNOLOGY, 208 (11) , p. 1681-1695.

DOI: 10.1080/00295450.2022.2073950

Handle: <http://hdl.handle.net/1942/37675>

Minimal detection time for localisation of radioactive hotspots in low and elevated background environments, using a CZT gamma-ray spectrometer

Lowie Brabants,^{a*†} Mattias Simons,^{a†} David De Schepper,^b Eric Demeester,^b Wouter Schroeyers^a

^a Hasselt University, CMK, NuTeC, Nuclear Technology - Faculty of Engineering Technology, Agoralaan Building H, B- 3590 Diepenbeek, Belgium

^b KU Leuven, Department of Mechanical Engineering, ACRO research group, Wetenschapspark 27, Diepenbeek 3590, Belgium

*E-mail: lowie.brabants@uhasselt.be

†Both authors contributed equally to the work

Minimal detection time for localisation of radioactive hotspots in low and elevated background environments, using a CZT gamma-ray spectrometer

This study determines the minimal detection time (*MDT*) needed for successful localisation of radioactive hot spots during nuclear decommissioning works. An automated XY stage, equipped with a CdZnTe (CZT) spectrometer, was used to identify and localise hotspots of ^{241}Am , ^{137}Cs , and ^{60}Co in a 1.7 by 1.7 m area. The stage served as a preliminary test platform for the development of an automated robotic characterization platform (ARCHER robot). The dependence of the *MDT* on the detector efficiency and background level was examined. For low background environments, the *MDT* for ^{137}Cs was 871 ms and resulted in an error on the source localisation of 14.21 mm and an error on the activity of 6.85%. For elevated background levels, the *MDT* increased to 15,526 ms. The ^{137}Cs source was localised with an error of 34.13 mm and an error on the source activity of -7.04%. The used *MDT* determination method offers a valuable approach for decreasing total scanning times whilst avoiding missing the presence of hot spots.

Keywords: radiation mapping, radiological hotspot localisation, CZT detector, minimal detectable activity, minimal detection time

I. INTRODUCTION

As more and more nuclear power reactors reach the end of their operational life, it is expected that nuclear decommissioning activities will increase in the next decades.^{1, 2} For defining an effective decommissioning strategy, detailed knowledge about the presence of radioactive contaminations and hotspots is required.

Nowadays, most of the radiological characterisations are still performed using labour-intensive manual methods.³ However, the use of robots is becoming increasingly popular in the nuclear field because the repetitive nature of nuclear measurements

allows automation. In environments with high radiation background levels, automation reduces operators dose-uptake. Early detection of hotspots and subsequent early removal will ensure compliance with the good practice of keeping dose exposure of workers as low as reasonably achievable (ALARA).^{4,5}

A number of different detectors can be used in combination with robotic platforms, such as conventional radiation detectors or gamma cameras. Gamma cameras can be divided into three categories based on the used measurement principle: pinhole cameras⁶, coded-aperture cameras⁷ and Compton cameras⁸. Each of these detectors have their own advantages and disadvantages.

Typically, pinhole cameras offer a wide energy range and good angular resolution, but are heavy, have a small field of view and have extremely low sensitivity. On the other hand, coded aperture cameras have a higher sensitivity as they use a coded mask with multiple holes arranged in a particular order, but they require an additional decoding step. They achieve similar characteristics to a pinhole camera in angular resolution and field-of-view. The third category, Compton cameras, make use of the kinematics of Compton scattering to localise radiation sources without using collimators. As a result, Compton cameras have an optimal field-of-view (up to 360°) and high energy resolution. A downside to the Compton cameras is that they have a limited angular resolution and are not able to localise gamma-rays with energies below 250 keV.⁹

Gamma cameras can localise hotspots from greater distances than conventional detectors and have the advantage that no movement of the camera is needed to localise radiation sources. On the other hand, gamma cameras often have low efficiency, need

shielding, give only limited useful information for characterisation purposes and suffer from pile-up effects or even failures in intense radiation fields.⁹

On the other hand, robotics can carry more traditional spectrometers and perform measurements in a scanning manner. This approach has the advantage that the spectrometric data can be used for characterization purposes and the detectors are also operable in high radiation environments. The downside is the repetitive nature of the measurement. This can however be automated with the use of a robotic platform.

Currently an automated robotic platform is being developed, called the ARCHER (Autonomous Robotic platform for CHaracterERisation) robot platform. It is designed to carry out automated characterisation measurements in high dose rate environments encountered during decommissioning operations. The platform consists of a mobile navigation unit on tracks and a robotic arm equipped with a lightweight CdZnTe (CZT) spectrometer to scan surfaces and create radiation maps in high background environments. Footage of the ARCHER platform in action can be found in footnote^a. The current research paper demonstrates the outcome of ARCHER project's first phase, which consist of optimising the radiological mapping approach (scanning procedure) for the robotic platform.

Multiple papers have already discussed the use of different robotic platforms to scan surfaces and localise radioactive sources. Examples are the localisation of hotspots with robotic manipulators^{10,11} Unmanned Ground Vehicles (UGV) or Unmanned Aerial

^a <https://www.youtube.com/watch?v=yP0H3m0rrAk>

Vehicles (UAV)¹²⁻¹⁵. These studies cover a range of different platforms, scanning methods to map surfaces, interpolation methods and radiation detectors.

In these automated approaches to hotspot localisation, it can be noticed that measurement times are often set at a fixed value, without further optimisation of the opted detection time. By using shorter detection times per measurement, the total scanning time of the region can be reduced. On the other hand, the shorter detection times can increase the risk of not detecting the radioactive source. In this case, the small amount of pulses can make it impossible to distinguish the signal from background radiation.^{16,17}

It can also be noted that the total counts per second or dose rate are often used to create heat maps and localise hotspots. Although this has been proven to be an efficient approach to localise sources, the downside to this approach is that no spectral data are measured. As a result, radionuclide identification is not possible. However, this identification can be especially useful to localise hotspots of key nuclides such as ⁶⁰Co and ¹³⁷Cs. These key nuclides are often used in radiological characterisations because they can be correlated with the activity of hard-to-measure radionuclides (such as ⁹⁰Sr or ³⁶Cl).^{18,19}

Additionally, the methods used in the cited papers were applied to areas with low background radiation levels. In real-life scenarios, hotspots often occur in areas within nuclear installations that have elevated backgrounds. Correctly localising sources in higher background radiation levels will be more complex and will also influence the

required detection time. In these environments, mapping on only total counts can lead to missing hotspots.

In order to optimize the scanning methodology that will be implemented in the ARCHER platform, the current research proposes a minimal detection time (*MDT*) methodology that is based on a Minimal Detectable Activity (*MDA*) calculation. The proposed method will optimise the detection time at each scanning point and lead to heat maps of spectral information in specific Regions of Interest (ROIs) instead of total spectral counts or dose rate. The proposed *MDT* method will also be evaluated for its robustness in scenarios with elevated background levels.

II. MATERIALS AND METHODS

In this paper, different gamma-emitting radioactive sources, respectively ^{241}Am , ^{137}Cs and ^{60}Co (with an activity of 392 kBq, 161 kBq and 20 kBq), were localised simultaneously with an automated XY stage. This stage was equipped with a CZT spectrometer and was used as a preliminary test platform for the ARCHER robot platform. The spectrometric capabilities of the CZT detector were used to localise the hotspots, identify the radionuclides and quantify their activity.

The scan pattern was a grid with a spacing of 10 cm between each measurement point. The detector was placed at a height of 5 cm from the scanned surface. At each point in the grid, the detector was stopped and a static measurement was performed with a detection time equal to a calculated *MDT*. The scan pattern of the XY stage was identical to the pattern performed by the ARCHER robot platform illustrated in footnote^a.

Instead of using the total counts in the spectrum, only the observed number of counts in different spectral regions of interest (ROIs) were used. The ROI counts were used to create heat maps of the total scanned area. These heat maps were used to make a rough estimation of the locations and the activity of the hotspot.

The *MDT* was determined based on an *MDA* calculation that uses the detector efficiency and a predetermined activity level to calculate the minimal required measurement time that leads to successful localisation of a hotspot with an adequate confidence level. As the *MDT* approach is also strongly dependent on the background (BKG) count rate within the ROIs, each measurement campaign was started by measuring the BKG for 5 min at a location away from any hotspots before the actual scanning procedure was started.

The performance of the *MDT* approach was tested for scans performed in a natural BKG situation as well as for environments with elevated BKG levels. Depending on the count rate in the ROIs, the *MDT* calculation was performed by using a Poisson distribution or a normal distribution. The elevated BKG scenarios were simulated by placing radioactive sources close to the CZT detector.

Detector characteristics, such as full energy peak efficiency (ϵ) and background (BKG) are the basis of the *MDT* approach and are discussed in section II.A. These quantities were determined before starting the scanning sequence of a surface. In section II.B, the *MDT* approach is covered for both low and elevated BKG situations and the impact of detection efficiency on the detection time is discussed. Section II.C. covers the methodology for creating heat maps.

II.A. Detector Calibration And Background

A Kromek™ GR1 spectrometer, containing a 1 cm³ CZT crystal was used²⁰. This detector was chosen because it is low in weight, making it suitable for usage in robotic manipulator arms that are restricted in payload^{21,22}. Another advantage is that it can operate at room temperatures without cooling, which is not the case for some other semiconductor spectrometers such as germanium detectors²³. The CZT detector also has a relatively good energy resolution of < 2.5% at 662 keV and a non-linearity of < 1%, which makes it suitable for radionuclide identification²⁴. The detector was operated with the default manufacturer settings. Before starting the scanning measurements, the detector was calibrated with an energy, shape and efficiency calibration.

As already stated, the goal of the scanning measurements was to create heat maps of ROIs instead of maps of total counts or dose rates. In order to determine these ROIs for specific energies, energy and shape calibrations according to ^{25, 26} were performed. In this paper, the used radionuclides in the hotspots were ²⁴¹Am, ¹³⁷Cs and ⁶⁰Co. As a result, the energy and shape calibration were used to determine the ROIs that are linked to the gamma-ray emissions of these three radionuclides. This resulted in a ROI at 59 keV that was used to map ²⁴¹Am and a ROI at 662 keV for ¹³⁷Cs. For ⁶⁰Co, only the ROI for the 1173 keV gamma-ray was used. ²⁴¹Am, ¹³⁷Cs, ⁶⁰Co, ¹³³Ba and ²²Na were used for the energy and shape calibration covering a wide energy range of the CZT detector.

In order to optimise the detection time and estimate hotspot activities, full energy peak efficiencies of the CZT detector were experimentally determined for the three ROIs. ϵ determinations can be performed in several ways, such as by Monte Carlo methods or

experimentally by measuring sources with known activity.^{27–29} In this paper, the latter was used. The ε was calculated following Eq. (1).

$$\varepsilon = \frac{N_c}{A t P_\gamma} \quad (1)$$

Where N_c is the net number of counts in the ROI (corrected for the background and continuum), A the activity of the source at the time of measurement, t the live measurement time and P_γ the gamma-ray emission probability.

The ε of the CZT detector was experimentally determined for different source-to-detector geometries. This was achieved by placing sources at different locations in the scanned surface, whilst keeping the detector at the same location at a detector height of 5 cm. The different source-to-detector geometries are illustrated in Fig. 1. For each of the indicated source locations in Fig. 1, measurements were performed until a minimum of 10,000 counts were registered in the ROI of interest, corresponding to a relative error in the counting statistics of 1%.

The ε measurements resulted in ‘efficiency matrices’ for 59 keV, 662 keV and 1173 keV. These matrices which contain the efficiencies for different source-to-detector locations. The efficiencies in the matrices are dependent on the source-to-detector distances and the energy dependence of the detector.

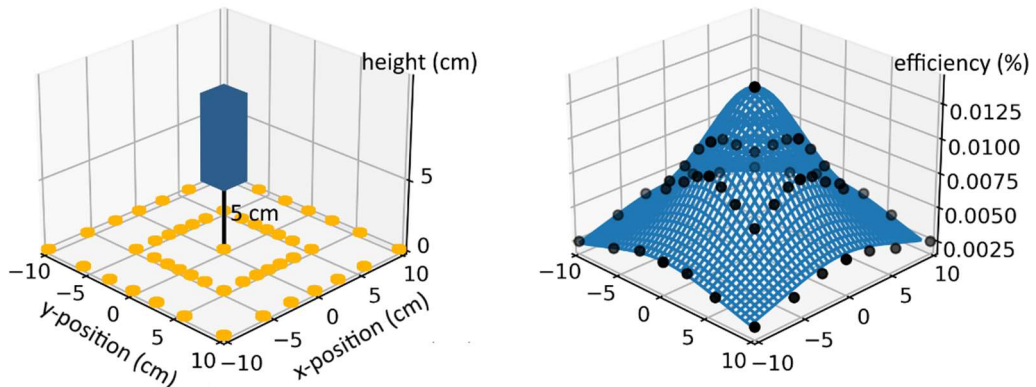


Figure 1. **Left:** source locations (indicated in yellow) that were used to determine the efficiency at 5 cm detector height. Measurements at all of the locations were used to determine a matrix of efficiencies. The measurements were performed for ^{241}Am , ^{137}Cs and ^{60}Co to obtain three efficiency matrices. **Right:** efficiency matrix for 662 keV. Black dots represent the efficiency values that were measured during the efficiency calibration. The blue wireframe represents the fitted relation between the detector efficiency at a specific energy and the X and Y positions of the source on the scanned surface.

The right-hand side of Fig. 1 shows the ε of 662 keV for the different source-to-detector geometries. The experimentally determined efficiencies are visualized as discrete black data points. These points match the source locations that are indicated on the left-hand side of Fig. 1. The discrete ε values, represented by black dots in Fig. 1, are fitted with a 3D least squares regression following the inverse square law, according to Eq. (2).

$$\varepsilon = \frac{a}{b^2 + x^2 + y^2} \quad (2)$$

In this equation, a and b are fitted parameters on the 3D plot and x and y represent the source positions on the scanned surface. The obtained fitted function is visualised in the right-hand side of Fig. 1 by a blue wireframe. The fitted function was used when sources were localised at positions where the efficiencies were not experimentally measured. The results of the fitted Eq. (2) at 59 keV, 662 keV and 1173 keV are listed in Table I. The energy dependence is illustrated in the fitted value of parameter a, which shows that the efficiency is the highest for 59 keV, followed by the efficiency for 662 keV and 1173 keV.

Table I. Fitted parameters for b and a for the efficiency values at 59 keV, 662 keV and 1173 keV.

	59 keV	662 keV	1173 keV
b	7.51	6.51	6.07
a	13.09	0.58	0.20

After the required calibrations were performed, a BKG measurement was performed at the start of each scanning pattern. A BKG measurement of 5 minutes was used to determine the detector response when no hotspot is present in the vicinity of the detector. This BKG measurement was important as i) this background level was used to determine the *MDT* and ii) the background signal was subtracted from the total peak area in a certain ROI to calculate the source activity after a hotspot was localised.

For the scans performed in elevated BKG environments, the following methodology was used to increase the BKG: the hot spot sources were placed directly underneath the detector in a normal BKG environment. The resulting count rates in the ROI of 59 keV, 662 keV and 1173 keV were measured. Next, this count rate was used as a reference value for increasing the BKG. After removing the hotspot sources from underneath the detector, a set of BKG sources containing ^{241}Am , ^{137}Cs and ^{60}Co was attached to the detector holder. They were placed at a distance which result in a count rate corresponding to 80% of the earlier determined count rate for each ROI. The resulting BKG level will be referred to as the 80% elevated or increased BKG. The 80% increased BKG was chosen as this was the most constraining BKG level that was practically achievable with the available sources. Although the count rates significantly increased when using the BKG sources, the dead time factor of the detector remained below 6% meaning that the total amount of dead time was always below 6% of the real time.

II.B. Minimal Detection Time

The detection time used for each measurement in the scan was determined with an *MDA* calculation. This calculation determines a detection time that is as short as possible, but still sufficient large to avoid missing the presence of a source. Conventionally, the *MDA*

calculation is performed in retrospect of a measurement performed with a certain measurement time. Calculating the *MDA* of such a measurement will provide information on the sensitivity limits of the measurement system. It is therefore often a regulatory requirement to report the *MDA* of a radiological analysis.

For the determination of the *MDT*, this approach was reversed. An *MDA* level was set at a predefined fixed value which was then used to calculate an *MDT*. When placing a hotspot in the scanned region, with an activity that exactly matches this *MDA*, the calculated *MDT* should be sufficient to localise the source, given a certain confidence level.

The first step in defining this measurement time was choosing the preferred *MDA* value. This can be interpreted as setting an activity limit above which a source is considered to be a hotspot. In each of the performed measurements, this activity limit was set at the exact activity of the used hotspot sources. Locations within a scanning area that contain radionuclides beneath this activity level should not be reported as a hotspot, whilst locations that are equal to or exceed this threshold should be identified as a region containing a hotspot. For this reason, the source activities on which the minimal required detection time was calculated were referred to as the *MDA*. The equation for calculating the *MDA* is:

$$LLD = MDA * \varepsilon * P_{\gamma} * MDT \quad (3)$$

Where *LLD* is the Lower Level of Detection, *MDA* is the activity of the source at the time of measurement, ε is the full energy peak efficiency of the CZT detector (in a specific ROI) for a source placed at a predefined distance from the detector (which is

derived from the efficiency matrix), P_γ the gamma-ray emission probability and MDT the minimal required detection time.

The dependence of the MDT on the choice of ε will be discussed in paragraph II.B.1. In addition to the ε , the MDT calculation is also based on calculating a correct value for LLD . Depending on the expected number of counts in a ROI, the calculation of the LLD was performed via a Poisson distribution for low counting statistics or via a normal distribution for higher counting statistics (see paragraphs II.B.2. and II.B.3.). This is directly related to the BKG levels. The LLD is the minimal number of net counts within the measured time above the background signal, within a ROI, that will be quantifiable, given a confidence level of 95%. The LLD is linked to the critical limit L_c , which is the net counts that must be exceeded in the measured time before the sample can be said to contain a statistically higher count rate than the background (again with a confidence level of 95%). L_c was not used in the calculation for the MDT . However, its value was used as a mask on the heat maps which is used to avoid visualisation of data that is not statistically different from the background.

The dependence of the MDT on the ε value and on the LLD (linked to the BKG levels) are further studied in the paper. The relation between MDT and source activity and P_γ are self-explanatory as sources with higher activities or higher P_γ values will require shorter detection times.

II.B.1. Efficiency

As ε is energy-dependent, the MDT value for different gamma-ray energies will also be different. As the ε for 59 keV photons is different from the ε of 662 keV and 1173 keV photons, the MDT will have a different value for ^{241}Am , ^{137}Cs and ^{60}Co . Measuring with

a detection time equal to the *MDT* calculated for ^{241}Am might not lead to the localisation of a hotspot of ^{137}Cs or ^{60}Co .

Additionally, ε depends on source-to-detector geometry. The ε of the detector is lower for sources placed further away from the detector, whereas for closer source-to-detector distances, the ε is higher. In other words, the value of the *MDT* will depend on which ε from the efficiency matrix is opted for.

As the hotspot's location is not known before starting the scan, it is impossible to know the exact ε value. This is opposite to the conventional application of the *MDA* approach in gamma spectrometry laboratories where samples are measured in a well-defined geometry. For this reason, a 'choice' or 'worst case estimation' with respect to the value of ε has to be made from the efficiency matrix geometries so that the *MDT* can be calculated.

An example is given for the scanning of an area where the *MDT* is determined from an ε for a source placed exactly in the middle of four measurement points of the 10 by 10 cm grid. This corresponds to the location X equal to 5 cm and Y equal to 5 cm (noted as [5;5]) from the projected centre of the detector on the floor surface on which the sources are located.

Imagine a source that is present which has an activity that exactly matches the *MDA* calculated from this [5;5] efficiency. This source will only be detected if it is located within a circular area of radius 7.07 cm around a measurement location, with a given confidence level of 95%. A circle is used to contour the area where a source with an

activity equal to the *MDA* can be detected (with a confidence level of at least 95%) as the efficiency matrix does not show any significant angular dependence of the CZT detector. Placing the same source outside of this ‘significance circle’ will not lead to a detection of the source with this confidence level. In this case, there would be a higher chance to not significantly detect the hotspot.

When choosing a worst-case efficiency of a source located 10 cm in the X direction and 10 cm in the Y direction (notes as [10;10]), this radius increases to 14.14 cm. The interpretation of the significance circle however remains the same: a source which has an activity that matches the *MDA* calculated from this ϵ at [10;10] can only be detected, given the confidence level of 95%, within this circle. Although the significance circle is larger for the ϵ at [10;10] (compared to the ϵ at [5;5]), the calculated *MDT* will be higher. As the scanning measurements were performed in a grid where each measurement is 10 cm apart, significance circles can be drawn around each measurement location. This is illustrated in Fig. 2 where significance circles are drawn for measurements performed with an *MDT* derived from an ϵ at [5;5] and an ϵ at [10;10].

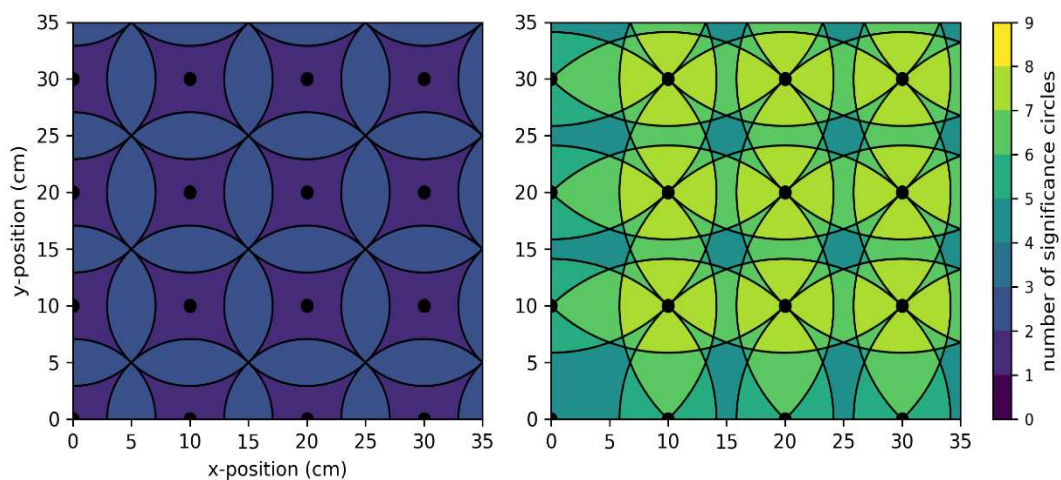


Figure 2. Significance circles drawn around measurement locations (black dots) for different ε values. **Left:** significance circles for ε values that match a source placed at [5;5]. **Right:** significance circles for ε values that correspond to a source placed at [10;10]. More overlap between the significance circles is observed when an ε value further away from the detector is used.

As only sources can be found with the desired confidence level within a significance circle, choosing an ε too close to the detector as ‘worst-case ε ’ may lead to not finding hotspots even though they are present. For an ε determined at [5;5], there is a relatively low overlap between circles of neighbouring measurement locations. In this case, when a source is situated in an area without any overlap, only one significant measurement will be achieved (within the 95% confidence interval) in the entire scanned region. As the source location is estimated by interpolation over multiple measurement points, having only one significant measurement point in the scanned region will lead to an inaccurate localisation of the source.

More overlap can be observed when scans are performed with an *MDT* calculated from the ε at [10;10]. In this case, there are always at least four significant measurement points (within the 95% confidence interval). This choice of a lower ε value will however increase the total scanning time. To make a correct choice in the ε used in the *MDT* calculation, measurements were performed with different *MDTs*. Efficiencies at [5;5] and [10;10] were used to evaluate the localisation performance for these different efficiencies.

The impact of the ε on the *MDT* was examined with the same experimental setup with regard to the used sources and source locations. In this case, the performance of the

hotspot localisation was evaluated when *MDTs* are calculated from different choices in the ε value.

II.B.2. LLD And L_c For Low Number of Counts

Next to the correct choice of the ε value, the calculation of a correct *LLD* value in Eq. (3) is crucial for determining an *MDT*. For a low number of counts (≤ 20 counts), the counts in a ROI follow a Poisson distribution. The *LLD* corresponds to the minimal number of net counts above the background within the detection time that will be quantifiable, given a false positive level of $p=0.05$ for a Poisson distribution. Values for *LLD* and L_c are tabulated in Ref. 13 for the Poisson distribution against the mean BKG counts in the measurement time.^{30,31}

For calculating the *MDT*, we take as an example a measurement aimed at localising a ^{137}Cs source in a low background environment. The BKG measurement yielded a very low BKG count rate of 0.01 cps within the ROI of 662 keV. Using the tabulated value in Ref. 13 for *LLD* of 3 counts, Eq. (3) was solved to determine an *MDT* of 871 ms. Within this detection time, an expected average of 0.00871 counts were due to the BKG. Next, this calculated *MDT* was used to start a scan and the tabulated value for L_c of 2 was used for the mask on the heat map.

II.B.3. LLD For Higher Number of Counts

For higher number of counts (>20 counts), the *LLD* has the same interpretation as for low count situations. However, this time it is related to a one-sided normal distribution. The *LLD* is given by Eq. (4).^{16,31,32}

$$LLD = k^2 + 2k \left[\frac{R_b}{t_b} \left(1 + \frac{t_b}{MDT} \right) \right]^{1/2} * MDT \quad (4)$$

Where k is the one-sided confidence factor of the normal distribution, MDT is the minimum count time required of the sample plus the background, t_b is the background count time, and R_b is the background count rate, which is determined from the background measurement.

Similar to the previous example, the MDT can be calculated but in this case for a ^{137}Cs source in a high background environment. The five-minute BKG measurement yielded a BKG count rate of 4369 cps within the ROI of 662 keV. Solving equations 3 and 4 resulted in a measurement time of 15,526 ms. The L_c which was used for the mask on the heat map was then determined following Eq. (5). The L_c for elevated background counting statistics, which was used in the applied mask of the heat maps is given by Eq. (5). For the above example, an L_c level of 251.48 counts was calculated.

$$L_c = 1.645 \left[\frac{R_b}{t_b} \left(1 + \frac{t_b}{MDT} \right) \right]^{1/2} * MDT \quad (5)$$

To summarise, the MDT is calculated from an LLD value which is determined from either a Poisson or a Normal distribution (depending on the BKG). This impact of the BKG on the MDT was examined by scanning an area that contains three hotspots (one hotspot of ^{241}Am , one hotspot of ^{137}Cs , and one hotspot of ^{60}Co) at known locations. The performance of the hotspot localisation is evaluated for low BKG and elevated BKG environments.

II.C. Heat Maps and Source Characterisations

The XY stage was able to perform measurements in a range of 1.7 x 1.7 meters and the detector was set at a constant height of 5 cm. In this surface three radioactive sources containing ^{241}Am , ^{137}Cs , ^{60}Co were placed at precisely known locations. A BKG

measurement was performed and the MDT was calculated. Next, the scanning was started and a spectrum was measured with a measurement time equal to the MDT .

After performing the scan, the sources were localised by creating 2D heat maps for each ROI. In these heat maps, the total counts at each discrete measurement point were interpolated with a Gaussian interpolation algorithm using a mesh of 1 by 1 mm. Within the heat maps, data points that were not significantly above the BKG were not visualised. A mask with value L_c was used to hide these insignificant data points. Application of the mask was chosen to avoid misinterpretation of the measured heat maps.

The interpolated data was used to calculate the source position by looking at the maximum of the interpolated matrix. The measurement point closest to the estimated source location was then used to calculate the activity of the source. To estimate this activity, a better estimate of the ε was interpolated from the fit on the efficiency matrix with the interpolated coordinates. The estimated source location and activity were then compared to the actual source location and source activity to evaluate the performance of the scanning approach.

III. RESULTS AND DISCUSSION

III.A. ROI Heat Maps

Heat maps are frequently created for total counts or dose rates. It is, however, possible that in situations with elevated backgrounds, this approach can lead to missing the presence of a hotspot. Fig. 3 illustrates the shortcomings of mapping only total counts. In Fig. 3, two scanning measurements were performed with a detection time of 871 ms.

One scan was performed in a normal BKG environment, and the second in an elevated BKG environment.

The elevated BKG environment was achieved by attaching an ^{241}Am source of 392 kBq to the detector at a distance of 5 cm from the centre of the CZT crystal. In the scanned region, a single ^{137}Cs hotspot was present. No calculation of the MDT or L_c was performed for these measurements as Fig. 3 is only intended to illustrate the limitations of using total counts for mapping purposes.

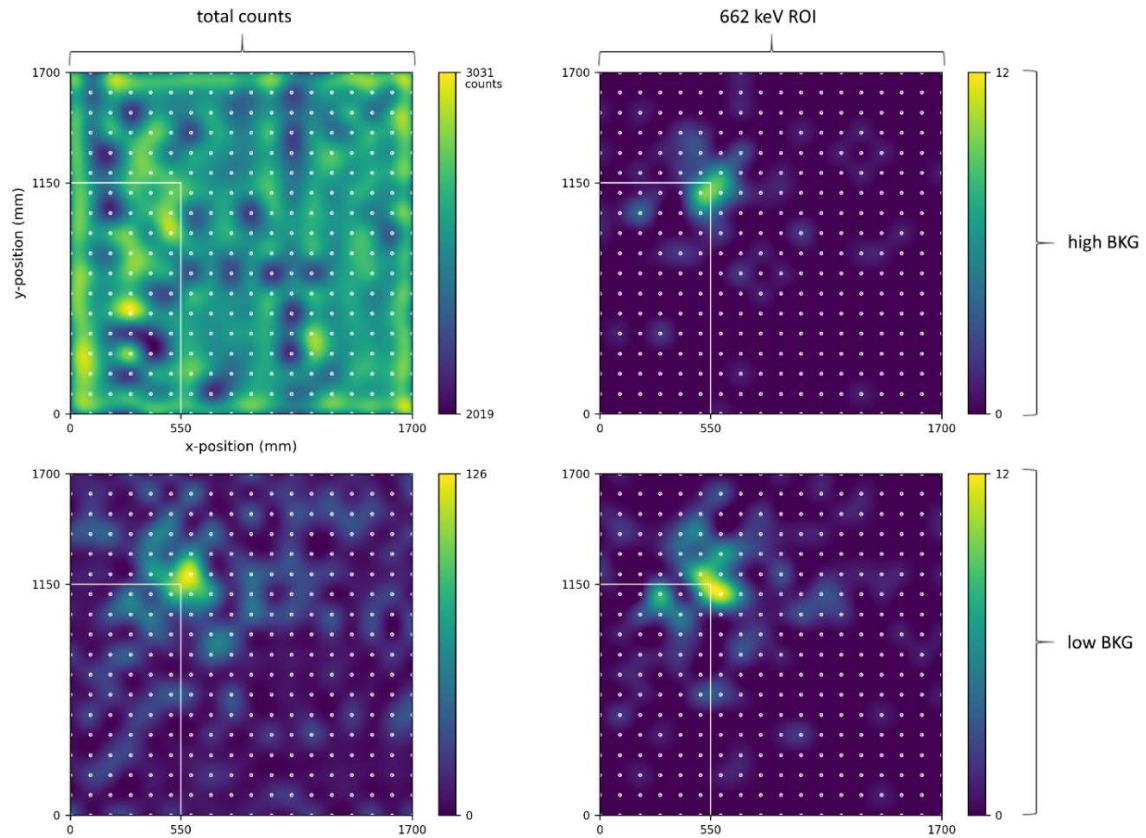


Figure 3. Heat maps of a surface containing a ^{137}Cs hotspot, measured with a detection time of 871 ms in two BKG environments. **Top row:** total counts (left) and of counts in the ROI of 662 keV (right) for an elevated BKG. **Bottom row:** total counts (left) and of counts in the ROI of 662 keV (right) for a normal BKG.

The bottom row of Fig. 3 gives the heat map of total counts (left) and the counts in the ROI of 662 keV (right) for a normal BKG level. It can be observed that both the total counts and the ROI heat map show the presence of the hotspot. The heat maps resulting from the scanning measurement performed in an elevated background are plotted in the top row. In this case, the heat map of the total counts (left) does not reveal the hotspot of ^{137}Cs , whereas the hotspot can clearly be localised in the heat map of the ROI of 662 keV.

With this BKG, creating heat maps of total counts, and only base the decision of the presence of a hotspot on total counts would give a false claim of absence of a hotspot in the scanned region. Heat maps of ROI data also have the added benefit of radionuclide identification and activity quantification. For these reasons, further heat maps will be plotted only on the basis of the ROIs and not of the total registered counts. The three ROIs that will be plotted in the next heat maps are the ROIs of 59 keV, 662 keV and 1173 keV.

III.B. Minimal Detection Time

III.B.1. Impact of Efficiency On MDT

The ε combines the source-to-detector distance and the energy dependence of the CZT detector. Fig. 4 illustrates the localisation performance when scans are performed with different detection times. The detection times are calculated from different choices in the ε value. The *MDT* per point was calculated based on the 662 keV ε resulting in a detection time of 340 and 871 ms respectively for a source placed at [5;5] and [10;10]. Additionally, a scan was performed with a detection time of 170 ms, corresponding to half of the [5;5] *MDT*.

Within the scanned area, three hotspots were present: ^{241}Am located at [1350;850], ^{137}Cs at [550;1150] and ^{60}Co at [710;540]). Only the results for the ROI of 662 keV are plotted in Fig. 4.

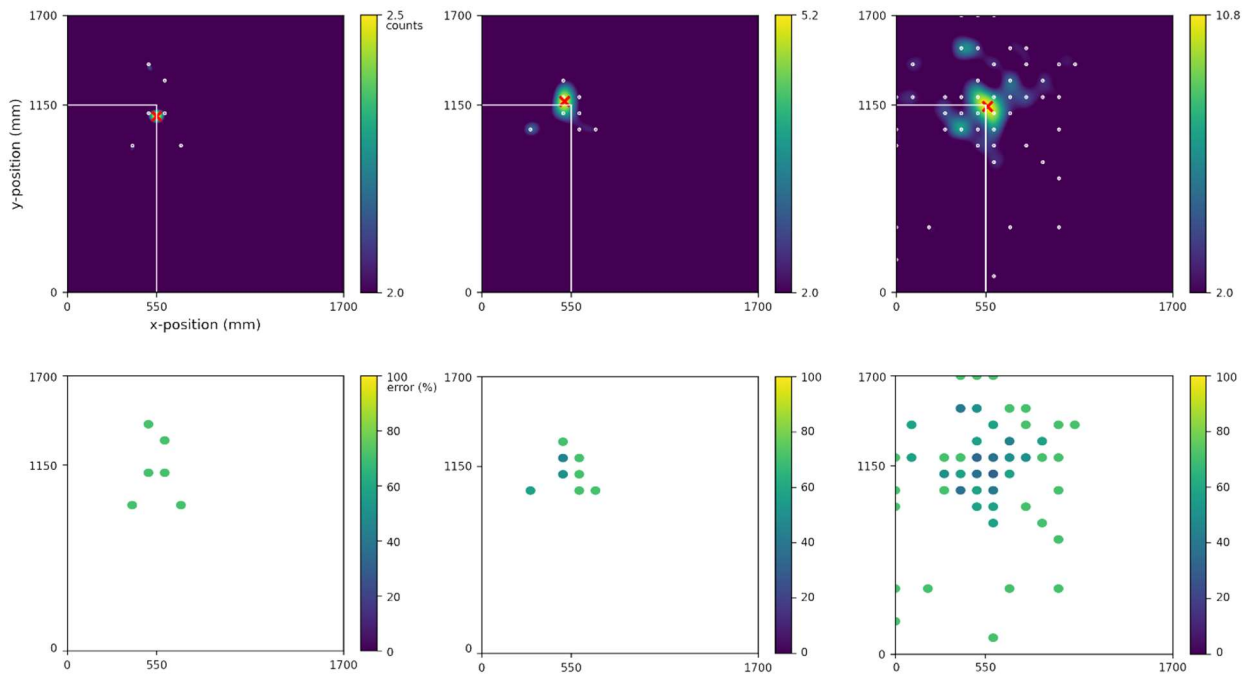


Figure 4. Heat maps, and corresponding statistical uncertainty of the ROI of 662 keV for measurements performed in normal BKG environments where ^{60}Co , ^{137}Cs and ^{241}Am are present in the scanned area. **Top row:** the number of significant measurement points increase (white dots) around the hotspot when the detection time is increased from 160 ms to 340 ms and 871 ms (left to right). With an increase in detection time, the interpolated ^{137}Cs source location (indicated by a red cross) also better matches the true ^{137}Cs source location (indicated by the white lines). **Bottom row:** more significant measurement points become apparent when the detection time increases from 160 ms to 340 ms and 871 ms (left to right). In addition, the percentage uncertainty on the counts (colour scale) decreases.

As the detection time increases from left to right, the width of the significance circles also increases. It can be observed that for measurements performed with a detection time of half the minimal detection time for an ε at [5;5], the hotspot is not missed.

However, less than four significant points (white dots) are measured surrounding the true source location. These points do not adhere to the 95% or higher confidence level required to be considered significantly above the background.

Only two significant measurement points were identified near the source in this scan. As a result, the interpolation localises the source on a straight line between the two significant points, leading to an error between the true and estimated location of 68.01 mm and an error on the activity of 2.49 %. It can be concluded that the set measurement time of 170 ms is insufficient. Scanning with this detection time did not lead to missing the hotspot. However, given the statistical nature of radioactivity, repeating the experiment might lead to situations where only one significant point is measured. This would lead to a very inaccurate localisation or, in some measurements, even lead to missing the hotspot completely.

For measurements performed exactly at the minimal detection time calculated from the ϵ at [5;5], the results show that, as expected from Fig. 2, the four surrounding measurements are significant. Some of the neighbouring data points can also be significant, but will not adhere to the same confidence limit of 95% of the four surrounding acquisition points. As more data points surrounding the source are significant, a more accurate localisation of the source and a better estimation of the hotspots activity is achieved. In this case, the source is localised with an error on the location of 47.89 mm and -7.30% on the source activity.

From the results of the measurement time of 340 ms, one might conclude that setting this detection time is sufficient for identifying the presence of a hotspot and for

accurately determining the location of the source. However, it should be considered that the sources were placed in the middle of the 10x10 cm grid, which is the most favourable position for scans performed with a measurement time derived from an ε for [5;5] (see Fig. 2). When sources are placed at a location where no significance circles overlap, only one measurement point will adhere to the 95% confidence limit. In this case, a similar scenario to the heat map of 170 ms would be the result, where the localisation and activity estimation would not be satisfactory.

In the last heat map was measured with an *MDT* calculated from the ε at [10;10]. Here, more significant measurement points are visible. This implies there is less chance to miss a hotspot, but although more significant points can be observed in the heat map, the performance of the localisation did not increase. The error on the localisation of 14.21 mm is comparable to the observed error for the scan performed with the [5;5] ε . Again, an explanation can be found in the placement of the hotspot in the middle of the 10x10 square. Looking at the significance circles for the ε at [5;5] and at [10;10], the same number of minimal overlapping significance circles is four for both scenarios for this hotspot location. But unlike the scans performed at [5;5] for which the placement in the middle of the 10x10 square of the sources was the most optimal, this source location is the most constraining location for scans performed with a detection time derived from an ε at [10;10]. If a hotspot was located directly beneath one of the measuring points, and an ε at [5;5] was used to calculate the *MDT*, only a single measurement point would adhere to the desired significance level.

To summarize, the worst-case localisation performance of scans performed with the ε of [10;10] matches the best-case localisation performance of scans performed with the ε of

[5;5]. Additionally, for scans that use a detection time derived from the ε at [10;10], a single measurement will be significant no matter where the source is placed in a single area of 10x10 cm. Adding to the information given in the heat maps, the uncertainties on the counting statistics is another factor that supports the decision of using the [10;10] ε as higher detection times lead to more registered counts, and hence better counting statistics. Having lower uncertainties on the counting statistics will be important as it will decrease the error on the localisation and on the estimation of the source activity.

Fig. 4 illustrates that the choice of the ε value will be a trade-off between the risk of not finding the source, the accuracy of the localisation, the uncertainties on the counting statistics and the measurement time. The ε at [10;10], will be used for the scanning measurements performed at elevated backgrounds. This ε was chosen as in our application more priority was given to the number of significant measurement points surrounding the hotspot compared to the increase in detection time. The time gain achieved by automating the scanning measurements outweighs the slightly larger detection time.

For applications where the total detection time is more important, the trade-off might lead to preferring shorter detection times. An additional aspect that leads to the choice of using the [10;10] ε is the fact that in a decommissioning situation, it is possible that the hotspot does not represent point sources and the activity is more spread over a surface rather than a point. In this case, the conservative detection time linked to the [10;10] ε will also lead to successful localisation of hotspots which are just below the set *MDA* used in the calculation of the *MDT*.

III.B.2. Impact Of Background On MDT

As illustrated in Fig. 3, the elevated BKG level provides a restriction in the use of total counts for plotting heat maps. Also, for heat maps of ROIs, the elevated background will make it more challenging to distinguish spectral peaks from the high background noise. To study the effect of the background on the *MDT*, scanning measurements were performed in normal background situations, and in elevated backgrounds. Fig. 5 shows heat maps of the ROI of 59 keV, 662 keV, and 1173 keV gamma-rays for the measurements with low and high backgrounds. The applied *MDTs* all calculated from the 662 keV [10;10] ϵ . The used *LLD* was calculated from the background count rates of either a 5 min natural BKG measurement or from a 5 min elevated BKG measurement. Three different combinations of BKG level and *MDTs* were analysed:

- a) Scan performed in a natural BKG with an *MDT* calculated from a 5 min natural BKG measurement (Fig. 5 top row);
- b) Scan performed in an elevated BKG with an *MDT* calculated from a 5 min natural BKG measurement (Fig. 5 middle row);
- c) Scan performed in an elevated BKG with an *MDT* calculated from a 5 min elevated BKG measurement (Fig. 5 bottom row).

The columns of Fig. 5 present heat maps of the ROI of 59 keV, 662 keV and 1173 keV. For each scan, the same sources and source locations were used as for Fig. 3.

Looking at the top row: as the scans were performed for detection times calculated for ^{137}Cs , it can be observed that the ^{241}Am source is localised easily as the 59 keV gamma-rays have a much higher ϵ than the ϵ of the 662 keV photons. The calculated *MDT* for ^{137}Cs is therefore larger than the *MDT* that would be required to localise the ^{241}Am

source. Additionally, the source activity of the ^{241}Am source is also much higher than the activity of the ^{137}Cs or the ^{60}Co source.

In this 59 keV heat map, the error on the source localisation was 29.02 mm and the error on the activity was 2.52%. The error on the location and activity of the source for the ^{137}Cs source was 14.21 mm and 6.85%. For the heat map of the ROI of 1173 keV, the detection time is insufficient to identify the ^{60}Co source which is a result of the low activity and low ε of the CZT detector for 1173 keV photons. The top row of Fig. 5 thus illustrates the dependency of the *MDT* on the gamma-ray energy and source activity.

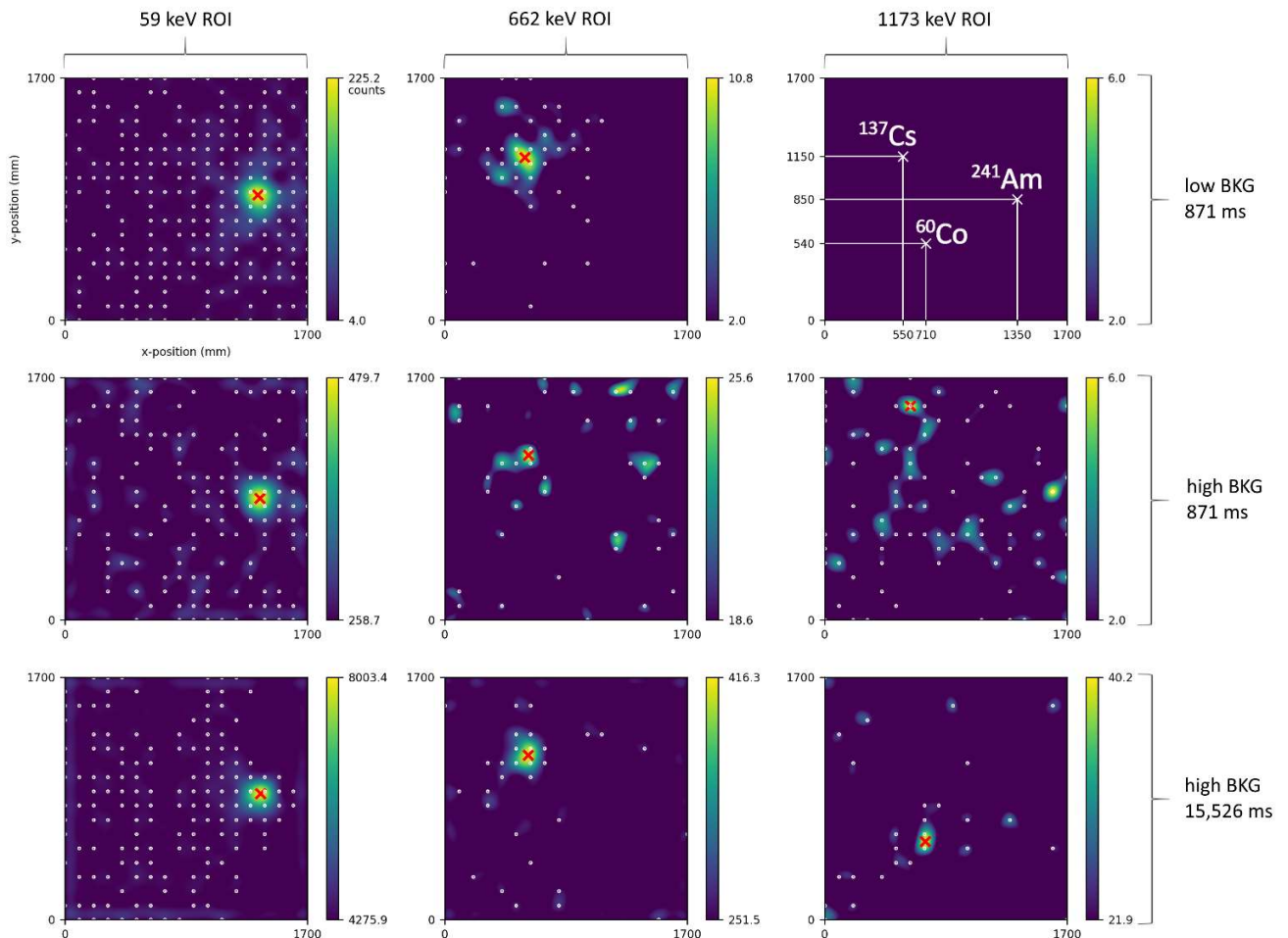


Figure 5. Scans performed with MDTs of ^{137}Cs , for low and elevated BKG levels. Heat maps are presented for the ROI of 59 keV, 662 keV and 1173 keV for a single setup with three hotspots present respectively of ^{60}Co , ^{137}Cs and ^{241}Am . From left to right, the columns of figures represent the ROI of 59 keV, 662 keV and 1173 keV. **Top row:** scan

in a normal BKG and a minimal detection time of 871 ms. **Middle row:** scan with a measurement time of 871 ms in an 80% elevated background. **Bottom row:** scan with an elevated BKG of 80% and a minimal detection time of 15,526 ms.

For the second row of heat maps, the same measurement time as for row 1 was applied. The measurements were however performed in an elevated BKG. It can be observed that even though the minimal detection time was calculated for ^{137}Cs in a normal BKG environment, the heat map still identifies the hotspot of ^{137}Cs . As there are only three significant measurement points, this heat map does not adhere to the predefined performance of a heat map as the intended criterion is to have at least four significant measurements surrounding the source. As a result, the applied detection time will lead to higher uncertainties on the counting statistics compared to measurements with an *MDT* that take into account the higher BKG level.

Similar to the first row, the ^{60}Co source was again not detected. For the ^{241}Am source, the detection time was sufficient and the source was located with an error of 15.52 mm and an error in source activity of 16.49%. This second row of heat maps illustrates the importance of the BKG on the calculation of the minimal required detection time. Elevated levels of BKG will increase the value of *LLD* in Eq. (2). The higher the BKG signal in a ROI, the longer the detection time must be in order to accumulate sufficient spectral counts to give a significant signal above the BKG.

Taking into account the elevated BKG in the calculation of the *MDT*, as is the case in the bottom row of Fig. 5, the heat map of the ROI of 662 keV is again able to successfully identify the hotspot of ^{137}Cs proving the applicability of the *MDA* approach also for elevated BKG levels. The ^{137}Cs source was localised with an error of 34.13 mm

and an error on the source activity of -7.04%. The errors for the localisation and source activity of ^{241}Am were respectively 41.34 mm and -17.75%. For ^{60}Co the hotspot was localised, but as only two measurement points were significant, the heat map also does not adhere to the predefined performance of a heat map as the applied detection time will not lead to four significant measurement points.

Fig. 5 covers the scanning patterns executed with an *MDT*, for localising ^{137}Cs , of 871 ms and 15,526 ms for respectively low and elevated BKGs. When calculating the *MDT* values based on the efficiencies and activities of the ^{241}Am and ^{60}Co source, the detection times would be 42 ms and 14,757 ms in a normal BKG environment. The high difference in *MDT* values for the different hotspot sources are expected results when looking at Eq. (3) as there is a big difference in source activities, P_γ , energy dependence of the ε , and BKG count rates. In the elevated BKG environment, these detection times would increase to 646 ms and 2,055,423 ms for respectively ^{241}Am and ^{60}Co .

III.C. Implementation to Other Platforms

The current research used an automated XY stage as a preliminary test platform before applying the methodology to the ARCHER platform. The used scanning settings, namely a detector height of 5 cm and scanning in grids of 10 x 10 cm were based on the desired design specification of the ARCHER platform.

The *MDT* approach however remains the same if it were to be applied for other source localisation applications using robotic arms, UAVs or UGVs. Also for other type of radiation detectors, the *MDT* approach remains valid. Depending on the application, other grid distances or detector heights can be opted for based on the desired level of

localisation accuracy. To apply this method, only the ε matrix will have to be changed to match the desired application.

Smaller grids would lead to more accurate localisations, but would also lead to more measurement points and hence longer total scanning times. In the case other scanning settings are applied, the ε matrix will have to be extended to include the desired detector height and scanning grid. Only ^{241}Am , ^{137}Cs and ^{60}Co were used in this study. If an application would require scanning for other key radionuclides, the *MDT* approach will however remain similar. Only the ε matrix will have to be determined for the ROI specific to the key radionuclide

IV. CONCLUSIONS AND OULOOK

This paper proposed a method to determine the *MDT* for the localisation of different radioactive hotspots of key radionuclides ^{241}Am , ^{137}Cs and ^{60}Co . The optimisation of the detection time is based on an *MDA* calculation that uses the detector efficiency and a predetermined activity level to determine the minimal required measurement time that leads to successful localisation of a hotspot with an adequate confidence level. The impact of using different detector efficiencies and using different levels of BKG on the *MDT* was studied by performing scanning measurements with an automated XY stage equipped with a CZT spectrometer. Scans were performed with a detector height of 5 cm in a grid pattern of 10 x 10 cm, covering a total surface of 1.7 x 1.7 meters.

Heat maps were created of the counts in three specific ROIs (of 59 keV, 662 keV and 1173 keV) as mapping total counts was found to be restrictive for elevated BKG environments. Mapping in ROIs also proved the added benefit of source identification and activity estimation of the hotspots.

A [10;10] ϵ was found to be the optimal efficiency value for the current research application as this ϵ value demonstrated a low risk of not finding the source, a good accuracy of the localisation and a low uncertainty on the counting statistics. For the used sources of ^{241}Am , ^{137}Cs and ^{60}Co (with an activity of 392 kBq, 161 kBq and 20 kBq) the calculated *MDTs* were respectively 42 ms, 871 ms and 15,526 ms. When scanning with the *MDT* of 871 ms, the ^{137}Cs hotspot was localised with an error of 14.21 mm and an error on the activity of 6.85%.

The impact of the background level was studied by artificially increasing BKG count rates. This was achieved by attaching different radioactive sources near the CZT detector. For the elevated BKG situations, the *MDT* calculated for the ^{137}Cs source of 871 ms for a normal BKG environment was insufficient to adequately locate the hotspot of ^{137}Cs .

When the *MDT* was calculated from the higher BKG environment, the ^{137}Cs source was again localised, with the desired confidence level, proving the *MDA* approach also for higher BKG. In the high BKG environment, the *MDT* of 15,526 ms localised the ^{137}Cs source with an error of 34.13 mm and an error on the source activity of -7.04%. The *MDT* for the ^{241}Am and ^{60}Co source in the high BKG environment was 646 ms and 2,055,423 ms.

For future works, the developed *MDT* approach will be applied to the ARCHER platform and tested during nuclear decommissioning works. With the ARCHER platform, operators can select planes on surfaces under investigation that can then be

characterised using an automated *MDT* approach. Future work will further examine the effect of using non-point source geometries on the proposed *MDT* approach. Also the dependence of the localisation performance for higher detection times will be further evaluated. As the current heat maps are determined on very low counting statistics, increasing the detection time will give better localisation performance which will have to be weighed against the increase in total scanning time. Also applying other interpolation algorithms will be the subject of future research.

Acknowledgments

Research was performed in the context of the ARCHER project, carried out by academic research partners UHasselt and KU Leuven in collaboration with the industrial partners EQUANS and Magics Instruments. This project is funded by the Energy Transition Fund of FOD economy (federal government Belgium). This work was also supported by the Fund for Scientific Research Flanders (FWO) scholarship nr 1SA2621N hosted by UHasselt and a BOF scholarship nr 60704300460004 of UHasselt. The authors would like to thank Samy Keymis and Levon Soghomonyan for their contributions to the development of the XY platform.

ORCID

Lowie Brabants: <https://orcid.org/0000-0003-1327-5196>

Mattias Simons: <https://orcid.org/0000-0003-1870-2599>

David De Schepper: <https://orcid.org/0000-0003-2090-0076>

Eric Demeester: <https://orcid.org/0000-0001-6866-3802>

Wouter Schroeiers: <https://orcid.org/0000-0001-9899-5269>

References

1. M. LARAIA, *Nuclear Decommissioning: Its History, Development, and Current Status*, in *Concrete* (London) **24** 1 (2018); <https://doi.org/10.1201/b15938-89>.

2. R. VOLK et al., “The future of nuclear decommissioning – A worldwide market potential study,” *Energy Policy* **124** August 2018, 226, Elsevier Ltd (2019); <https://doi.org/10.1016/j.enpol.2018.08.014>.
3. S. BODEN, B. ROGIERS, and D. JACQUES, “Determination of ¹³⁷Cs contamination depth distribution in building structures using geostatistical modeling of ISOCS measurements,” *Appl. Radiat. Isot.* **79**, 25, Elsevier (2013); <https://doi.org/10.1016/j.apradiso.2013.04.028>.
4. J. KAULARD and B. BRENDEBACH, “Radiation Protection during Decommissioning of Nuclear Facilities – Experiences and Challenges,” 14 (2005).
5. J. KIM and B. TSEREN, “Occupational alara planning for reactor pressure vessel dismantling at kori unit 1,” *Int. J. Environ. Res. Public Health* **17** 15, 1 (2020); <https://doi.org/10.3390/ijerph17155346>.
6. O. GAL et al., “CARTOGAM - a portable gamma camera for remote localization of radioactive sources in nuclear facilities,” *Nucl. Instruments Methods Phys. Res. Sect. A Accel. Spectrometers, Detect. Assoc. Equip.* **460** 1, 138 (2001); [https://doi.org/10.1016/S0168-9002\(00\)01108-6](https://doi.org/10.1016/S0168-9002(00)01108-6).
7. K. AMGAROU et al., “A comprehensive experimental characterization of the iPIX gamma imager,” *J. Instrum.* **11** 8 (2016); <https://doi.org/10.1088/1748-0221/11/08/P08012>.
8. C. G. WAHL et al., “Polaris-H measurements and performance,” 2014 IEEE Nucl. Sci. Symp. Med. Imaging Conf. NSS/MIC 2014, 3, IEEE (2016); <https://doi.org/10.1109/NSSMIC.2014.7431109>.
9. A. MARGARITA et al., “Recommended in situ measurement techniques for each constrained environment” (2020).

10. A. SELIVANOVA et al., “The use of a CZT detector with robotic systems,” *Appl. Radiat. Isot.* **166**, 109395, Elsevier Ltd (2020);
<https://doi.org/10.1016/j.apradiso.2020.109395>.
11. S. R. WHITE et al., “Radiation Mapping and Laser Profiling Using a Robotic Manipulator,” *Front. Robot. AI* **7**, 499056, Frontiers Media S.A. (2020);
<https://doi.org/10.3389/frobt.2020.499056>.
12. A. H. ZAKARIA et al., “Development of Autonomous Radiation Mapping Robot,” in *Procedia Computer Science* **105**, pp. 81–86, Elsevier B.V. (2017);
<https://doi.org/10.1016/j.procs.2017.01.203>.
13. N. A. ABD RAHMAN et al., “Mobile robot for radiation mapping in indoor environment,” *IOP Conf. Ser. Mater. Sci. Eng.* **785** 1 (2020);
<https://doi.org/10.1088/1757-899X/785/1/012021>.
14. B. LI et al., “Use of multi-rotor unmanned aerial vehicles for radioactive source search,” *Remote Sens.* **10** 5 (2018); <https://doi.org/10.3390/rs10050728>.
15. D. CONNOR, P. G. MARTIN, and T. B. SCOTT, “Airborne radiation mapping: overview and application of current and future aerial systems,” *Int. J. Remote Sens.* **37** 24, 5953 (2016); <https://doi.org/10.1080/01431161.2016.1252474>.
16. J. E. MARTIN, *Physics for Radiation Protection*, in *Physics for Radiation Protection* (2013); <https://doi.org/10.1002/9783527667062>.
17. G. R. GILMORE, *Practical Gamma-ray Spectrometry* (2008);
<https://doi.org/10.1002/9780470861981.ch16>.
18. A. PHYSICS, “The free release of the materials resulting from the decommissioning of the VVR-S research reactor,” 133 (2013).
19. IAEA, “Determination and Use of Scaling Factors for Waste Characterization in Nuclear Power Plants,” 124 (2009).

20. KROMEK, “Kromek GR-1A and GR1 the world’s smallest and highest resolution room temperature gamma-ray spectrometers” (2016).
21. Y. VERBELEN et al., “Miniaturised Low-Cost Gamma Scanning Platform for Contamination Identification, Localisation and Characterisation: A New Instrument in the Decommissioning Toolkit,” *Sensors MDPI* 2021, Vol. 21, Page 2884 **21** 2884, 187 (2021); <https://doi.org/10.3390/s21082884>.
22. M. KAZEMEINI et al., “Integration of CZT and CLYC radiation detectors into robotic platforms using ROS,” *AIP Conf. Proc.* **2160** October (2019); <https://doi.org/10.1063/1.5127711>.
23. P. M. JOHNS and J. C. NINO, “Room temperature semiconductor detectors for nuclear security,” *J. Appl. Phys.* **126** 4, AIP Publishing LLC (2019); <https://doi.org/10.1063/1.5091805>.
24. Y. TANIMURA et al., “Characteristics of commercially available CdZnTe detector as gamma-ray spectrometer under severe nuclear accident,” *Prog. Nucl. Sci. Technol.* **6** 0, 134, The Atomic Energy Society of Japan (2019); <https://doi.org/10.15669/pnst.6.134>.
25. ISO, “ISO 20042:2019 Measurement of radioactivity — Gamma-ray emitting radionuclides — Generic test method using gamma-ray spectrometry.”
26. CANBERRA, “Genie™ 2000 Spectroscopy Software - Operations Manual” (2000).
27. L. BRABANTS et al., “Validation of TOPAS MC for modelling the efficiency of an extended-range coaxial p-type HPGe detector,” *Appl. Radiat. Isot.* **173** November 2020 (2021).
28. G. S. CEBASTIEN JOEL et al., “Monte Carlo method for gamma spectrometry based on GEANT4 toolkit: Efficiency calibration of BE6530 detector,” *J.*

- Environ. Radioact. **189** April, 109, Elsevier (2018);
<https://doi.org/10.1016/j.jenvrad.2018.03.015>.
29. G. XHIXHA et al., "Calibration of HPGe detectors using certified reference materials of natural origin," J. Radioanal. Nucl. Chem. **307** 2, 1507 (2016);
<https://doi.org/10.1007/s10967-015-4360-6>.
30. J. L. ALVAREZ, "Poisson-based detection limit and signal confidence intervals for few total counts," Health Phys. **93** 2, 120 (2007);
<https://doi.org/10.1097/01.HP.0000261331.73389.bd>.
31. L. A. CURRIE, "Limits for Qualitative Detection and Quantitative Determination: Application to Radiochemistry," Anal. Chem. **40** 3, 586 (1968);
<https://doi.org/10.1021/ac60259a007>.
32. J. M. KIRKPATRICK, R. VENKATARAMAN, and B. M. YOUNG, "Minimum detectable activity, systematic uncertainties, and the ISO 11929 standard," J. Radioanal. Nucl. Chem. **296** 2, 1005 (2013); <https://doi.org/10.1007/s10967-012-2083-5>.